

# Detection of GeV $\gamma$ -Ray Emission from supernova remnant SNR G15.9+0.2 with Fermi-LAT

Yunchuan Xiang<sup>\*</sup>, Zejun Jiang<sup>†</sup> and Mengyao Tang

*Department of Astronomy, Key Laboratory of Astroparticle Physics of Yunnan Province, Yunnan University, Kunming 650091, China*

29 October 2021

## ABSTRACT

We first report GeV  $\gamma$ -ray emission from supernova remnant (SNR) G15.9+0.2 in this work. The results show that its power-law spectral index is  $2.94 \pm 0.25$  with a  $6.47\sigma$  significance level, and the  $\gamma$ -ray emission can be characterized by a two-dimensional (2D) Gaussian spatial distribution, which has a better improvement than the case of a point source. Moreover, we find that its likely counterparts from the radio, X-ray, and TeV energy bands are well coincident with its spatial location. We suggest that the new  $\gamma$ -ray emission may originate from SNR G15.9+0.2. On this basis, we discussed the probable origins of its  $\gamma$ -ray radiation.

**Key words:** ISM: supernova remnants - gamma-rays: diffuse background - radiation mechanisms: non-thermal

arXiv:2103.07824v7 [astro-ph.HE] 13 Aug 2021

<sup>\*</sup> E-mail: xiang\_yunchuan@yeah.net

<sup>†</sup> E-mail: zjjiang@ynu.edu.cn

## 1 INTRODUCTION

SNR is considered to be an efficient cosmic-ray factory. After the explosion of SNR, it is considered that the 10% kinetic energy of SNR transferred to CRs, and the maximum energy of cosmic-ray particles can be accelerated to approximately  $10^{15}$  eV through the diffusive shock acceleration mechanism (Bell 1978; Blandford & Eichler 1987; Drury et al. 1994; Morlino & Caprioli 2012). Their multiband spectra exhibit a typical bimodal structure through leptonic or/and hadronic processes (e.g., Zeng et al. 2019, 2021). For the radio-to-X-ray band, it is generally recognized that synchrotron radiation dominates (Allen et al. 1997, 1999; Uchiyama et al. 2007). For the GeV-to-TeV energy band, inverse Compton scattering and bremsstrahlung of relativistic electrons are generally considered to be important mechanisms (Vink 2012). In addition, decay of neutral pions produced in the inelastic hadronic interaction becomes more and more important to explain the GeV and TeV emissions of SNRs (e.g., Xin et al. 2017, 2019; Yang et al. 2021; Xiang & Jiang 2021). Detection of GeV  $\gamma$ -ray emission of SNR is very important for evaluating SNR's contribution to cosmic-ray flux in Milky Way (Acero et al. 2016), and it can also help us explore the acceleration mechanism of cosmic-ray particles and limit the energy distribution of accelerated particles, which provides further understanding of the evolution process of cosmic-ray particles in SNRs (Zhang & Fang 2007; Finke & Dermer 2012; Tang et al. 2013). Thus far, only 24 SNRs have been firmly certified in the Fermi Large Telescope Fourth Source Catalog (4FGL; Abdollahi et al. 2020). Therefore, more GeV SNRs are required to recognize the nature of particle acceleration within SNRs.

Caswell et al. (1982) found a clear shell structure from SNR G15.9+0.2 at 1415 MHz with about  $58''$  resolution using the Fleurs synthesis radio telescope. Based on the observations at 327.5 MHz and 1425 MHz from the NRAO VLA sky survey (NVSS), Dubner et al. (1996) found that the eastern border of SNR G15.9+0.2 had a bright shell feature; the northwest edge had two fainter knots; the north of the shell appeared an extension region of the radio emission with a  $3\sigma$  noise level at 1425 MHz. Through XMM-Newton observations, Maggi & Acero (2017) found the evidence of spatial variations by measuring the Fe K line features. They believed that SNR G15.9+0.2 with the lowest Fe K centroid energy is the core-collapse SNR. Moreover, they identified ejecta emission from this SNR by observing the Fe K line features. They identified that the progenitors of SNR G15.9+0.2 originated from a massive star, according to the observation the abundance ratios of Ca, Ar, S, Si, and Mg.

For the GeV band data, Acero et al. (2016) did not find significant GeV  $\gamma$ -ray emission of the SNR in the 1-100 GeV energy band using the Fermi Large Area Telescope (Fermi-LAT), and they provided its upper limits with the 95% and 99% confidence level for the power-law spectral indices of 2.0 and 2.5, respectively. For the TeV energy band, H.E.S.S. Collaboration (2018) introduced the TeV source HESS J1818-1542. They provided an upper limit of the photon flux in the 1-10 TeV band, which is  $2.6 \times 10^{-13} \text{ cm}^{-2} \text{ s}^{-1}$  with a  $3.7\sigma$  significance level. Although the distance between HESS J1818-1542 and SNR G015.9+00.2 is the closest than other TeV sources, there is a large angle separation with  $0^\circ.5$  between their positions. Therefore, their relevance is uncertain thus far. Abeysekera et al. (2017) found that the TeV source 2HWC J1819-150 is closer to SNR G15.9+0.2 with a position separation of  $0^\circ.1$ . In addition, the differential flux at 7 TeV is  $5.90 \pm 0.79 \times 10^{-15} \text{ TeV}^{-1} \text{ cm}^{-2} \text{ s}^{-1}$  with a spectral index of  $-2.88 \pm 0.10$ .

In this study, for the improvement and accumulation from the Fermi-LAT Pass 8 data and the update of  $\gamma$ -ray background models from galactic diffuse emission and the isotropic extragalactic emission (Abdollahi et al. 2020), the GeV  $\gamma$ -ray emission of SNR G15.9+0.2 was reanalyzed using approximately 12.4 years of the Pass 8 data. In the preliminary analysis, a likely GeV  $\gamma$ -ray emission from the region of SNR G15.9+0.2 was found, which strongly inspired us to explore the characteristics and origin of this GeV  $\gamma$ -ray emission in this study. Subsequent works include the introduction of data reduction in Section 2, the presentation of the analysis results in Section 3, and the discussion and conclusion about the likely origins of the GeV radiation in Section 4.

## 2 DATA REDUCTION

Using FermiTools version v11r5p3<sup>1</sup>, we analyzed the GeV  $\gamma$ -ray emission from the region of SNR G15.9+0.2 by selecting the instrumental response function (IRF) "P8R3\_SOURCE\_V3" and the Pass 8 "Source" event class (evtype = 3 and evclass = 128). The observation period was selected to be from August 4, 2008, to December 29, 2020 (mission elapsed time (MET) 239557427-630970757). The energy range was selected to be 1-500 GeV to reduce contamination from the galactic diffuse emission for a large point spread function in the low-energy band. Photon events with the maximum zenith angles of  $90^\circ$  were selected to suppress the pollution from the Earth Limb. A  $20^\circ \times 20^\circ$  region of interest (ROI), centered at the position from SIMBAD (R.A., decl.=  $274^\circ.72, -15^\circ.03$ )<sup>2</sup>, was selected for this analysis. We selected the script `make4FGLxml.py`<sup>3</sup> to generate a source model file, and sources from the 4FGL within the ROI of  $30^\circ$  were included in the model file. Then, we included a point source with a power-law spectrum at the SIMBAD location of SNR G15.9+0.2 to the model file. The binned likelihood tutorial<sup>4</sup> was followed in the analysis. Furthermore, spectral indexes and normalizations from sources within the  $5^\circ$  range of the ROI were set as free in the model file. The normalizations from the isotropic extragalactic emission (`iso_P8R3_SOURCE_V3_v1.txt`) and the galactic diffuse emission (`gll_iem_v07.fits`)<sup>5</sup> were also set as free.

<sup>1</sup> <http://fermi.gsfc.nasa.gov/ssc/data/analysis/software/>

<sup>2</sup> <http://simbad.u-strasbg.fr/simbad/>

<sup>3</sup> <https://fermi.gsfc.nasa.gov/ssc/data/analysis/user/>

<sup>4</sup> [https://fermi.gsfc.nasa.gov/ssc/data/analysis/scitools/binning\\_likelihood\\_tutorial.html](https://fermi.gsfc.nasa.gov/ssc/data/analysis/scitools/binning_likelihood_tutorial.html)

<sup>5</sup> <http://fermi.gsfc.nasa.gov/ssc/data/access/lat/BackgroundModels.html>

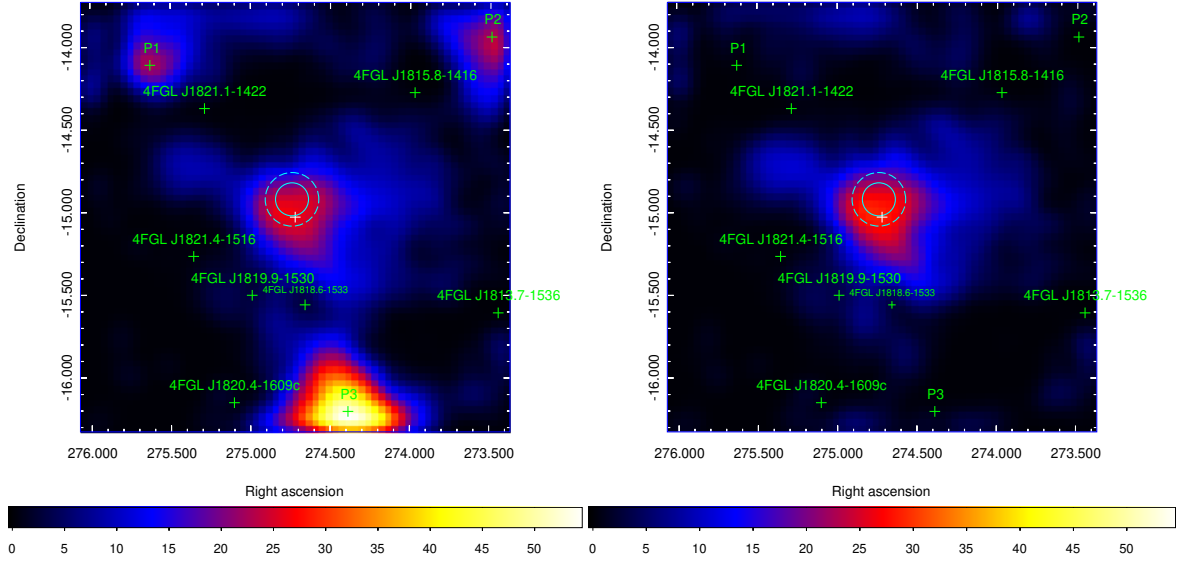


**Figure 1.** These TS maps of  $2^\circ.6 \times 2^\circ.6$ , which were smoothed with a Gaussian function with a kernel radius of  $0^\circ.3$ , in the 1-500 GeV energy band with a  $0^\circ.04$  pixel size centered at the SIMBAD position of SNR G15.9+0.2 marked as a white cross. The 68% and 95% error circles of the best-fit position of this SNR are marked by using solid and dashed cyan circles in these TS maps, respectively. Left panel: TS map including all the 4FGL sources and the residual radiations in the region. **Right panel:** TS map after deducting three  $\gamma$ -ray excesses including P1-P3.

### 3 SOURCE DETECTION

Running the command `gt tsmap`, the test statistic (TS) map, which is centered at the SIMBAD location of SNR G15.9+0.2 in the 1-500 GeV energy band, was first calculated in this analysis. In the left panel of Figure 1, significant  $\gamma$ -ray radiation with a TS value = 30.20 was found in the region of SNR G15.9+0.2. Here, the TS value, defined as  $TS = 2\log(L_1/L_0)$  from (Mattox et al. 1996), is calculated to quantify a significant source, and  $L_1$  and  $L_0$  represent maximum-likelihood values;  $L_1$  contains target source;  $L_0$  does not contain. In addition, we identified three significant  $\gamma$ -ray excesses from the locations of P1, P2, and P3. Then, we chose to add these three point sources, with power-law spectra in the local maxima of the TS map, to their locations<sup>6</sup> to subtract the three significant residual emissions within the  $2^\circ.6 \times 2^\circ.6$  TS map for all subsequent analyses. As shown in the **right** panel of Figure 1, the  $\gamma$ -ray radiation was still significant with the TS value of 29.61 in the region of SNR G15.9+0.2.

To further confirm that the region of SNR G15.9+0.2 does not have other significant  $\gamma$ -ray residual radiations within the  $2^\circ.6 \times 2^\circ.6$  TS map, we also deducted the emission from the region of SNR G15.9+0.2. Using `gt findsrc`, we obtained the best-fit position of SNR G15.9+0.2 to be (R.A., decl. =  $274^\circ.74, -14^\circ.92$ ) with a 68% (95%) error circle of  $0^\circ.10$  ( $0^\circ.16$ ) by assuming a point source with a power-law spectrum at its SIMBAD location. As shown in Figure 2, we found its contours of the 1.4 GHz radio and X-ray energy bands are all within the 68% and 95% error circles of the best position of SNR G15.9+0.2. Moreover, the region with a  $1\sigma$  statistical uncertainty from the location of the TeV source 2HWC J1819-150 (R.A., decl. =  $274^\circ.83, -15^\circ.06$ ; from Abeysekara et al. (2017)) well overlaps with all the regions from three different energy bands. This indicates that these four sources from the radio to TeV bands are likely to be counterparts of SNR G15.9+0.2.

Using the uniform disk and two-dimensional (2D) Gaussian templates, we tested the different values of the radius and  $\sigma$ , which range from  $0^\circ.1$  to  $1^\circ.5$  with an increment of  $0^\circ.05$ , to obtain the probable  $\gamma$ -ray spatial distribution of the new source. Then, we calculated the value of the  $TS_{\text{ext}}$ , using the formula of  $2\log(L_{\text{ext}}/L_{\text{ps}})$  from Lande et al. (2012), where  $L_{\text{ps}}$  and  $L_{\text{ext}}$  represent the maximum log-likelihood values for the point source template and **extended** templates, respectively. **We found that the 2D Gaussian template has a significant improvement with the highest value of  $TS_{\text{ext}}$  and a  $\sigma$  of  $0^\circ.45$  in the analysis. Therefore, we adopted the 2D Gaussian spatial template with a  $\sigma$  of  $0^\circ.45$  as the best spatial template to analyze the new  $\gamma$ -ray source in all subsequent analyses.** The best-fit results with the highest TS values from the different templates were presented in Table 1.

#### 3.1 Spectral Analysis

In this analysis, we generated the spectral energy distribution (SED) in the 1-500 GeV energy band using a power-law spectrum model **with the formula,  $dN/dE = N_0 E^{-\Gamma}$ , and the 2D Gaussian template** for the new  $\gamma$ -ray source. **The result of the global fit is  $\Gamma = 2.94 \pm 0.25$ ;**

<sup>6</sup> The location of P1: (R.A., decl.= $275^\circ.63, -14^\circ.11$ ); that of P2: (R.A., decl.= $273^\circ.49, -13^\circ.99$ ); that of P3: (R.A., decl.= $274^\circ.39, -16^\circ.21$ ).

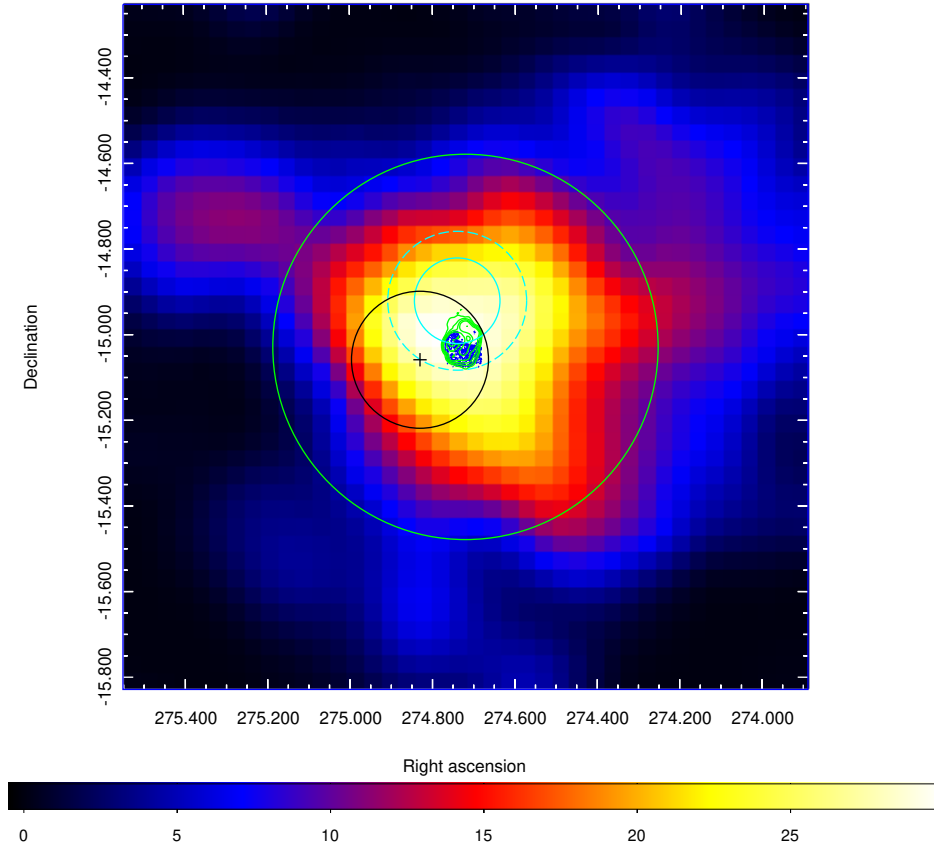


**Figure 2.** TS map of the region of  $1^\circ.6 \times 1^\circ.6$  is smoothed with a Gaussian kernel of  $0^\circ.3$  with a  $0^\circ.04$  pixel size in the 1-500 GeV energy band centered at the SIMBAD position of SNR G15.9+0.2. Two solid and dashed cyan circles were introduced in Figure 1. The green contours are from 1.4 GHz observations of NVSS (Caswell et al. 1982), and the blue contours are from X-ray observations of XMM-Newton (Maggi & Acero 2017). A black cross represents the position (RA=274°.83, decl.=-15°.06) of 2HWC J1819-150, and its  $1\sigma$  statistical uncertainty of this position is  $0^\circ.16$ , which is represented by a solid black circle (Abeysekara et al. 2017). The green circle indicates the extent of the GeV emission (2D Gaussian template) in this work.

**Table 1.** Spatial Distribution Analysis for SNR G15.9+0.2 with Different Spatial Models in The 1-500 GeV Energy Band

Spatial Model	Radius ( $\sigma$ ) degree	Spectral Index	Photon Flux $10^{-9}$ ph cm $^{-2}$ s $^{-1}$	TS Value	TS <sub>ext</sub>	Degrees of Freedom
Point source	-	2.94±0.51	0.39±0.10	29.61	-	4
2D Gaussian	0°.45	2.94±0.25	4.09±0.57	55.67	26.06	5
uniform disk	0°.75	2.96±0.23	3.62±0.53	50.93	21.32	5

$N_0 = (1.04 \times 0.15) \times 10^{-12}$ ; its photon flux is  $(4.09 \pm 0.57) \times 10^{-9}$ ph cm $^{-2}$  s $^{-1}$ . The SED was divided into 10 equal logarithmic bins. Each energy bin was fitted using the binned likelihood analysis method. For the energy bins with the TS value  $< 4$ , we calculated their upper limits with a 95% confidence level. Considering the subsequent energy bins with large statistical errors and the TS values  $< 4$ , here we selected to provide two upper limits for the SED, as shown in Figure 3.

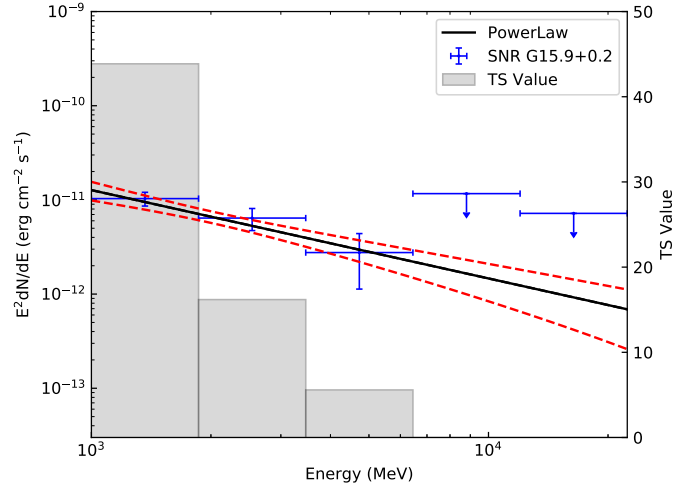


**Figure 3.** The SED of SNR G15.9+0.2 from the 1 GeV to 500 GeV energy band. Blue points indicate the result of the Fermi-LAT observation with the  $1\sigma$  statistical uncertainties. The black solid line represents the result of the global fit with a power-law spectral model, and the two red dashed lines represent the  $1\sigma$  statistical uncertainties of the global fit. The gray shaded areas represent the TS value of each energy bin. For the energy bins with TS values  $<4$ , the upper limits with a 95% confidence level are given.

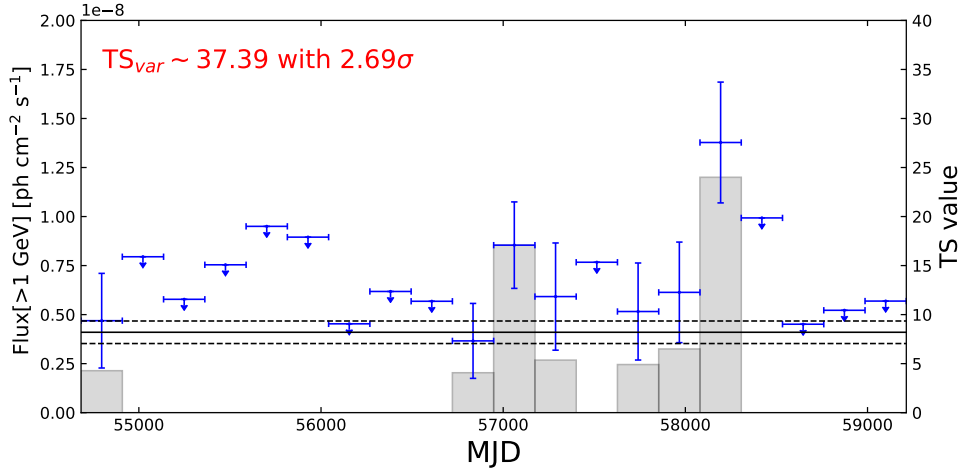


**Figure 4.** LC of SNR G15.9+0.2 with 20 time bins in the 1-500 GeV band. For the time bins with TS values  $<4$ , the upper limits with a 95% confidence level are given. The gray shaded areas show the TS value of each time bin. The black solid line and the two black dashed lines are used to show the average photon flux from the maximum likelihood fit and its  $1\sigma$  statistical uncertainties, respectively.

### 3.2 Variability Analysis

To check the variability of the photon flux over 12.41 years for the new  $\gamma$ -ray source, we generated a light curve (LC) with 20 time bins in the 1-500 GeV energy band, as can be seen from Figure 4. Calculating the variability index  $TS_{var}$  defined by Nolan et al. (2012), we acquired  $TS_{var} = 37.39$  with a  $2.69\sigma$  variability significance level<sup>7</sup>. The result implies that the new  $\gamma$ -ray source exhibits a **hint of weak variation**<sup>8</sup>.

<sup>7</sup> Here, the variability significance level is calculated by the SciPy package (Virtanen et al. 2020).

<sup>8</sup>  $TS_{var} \geq 36.19$  was used to identify variable sources at a 99% confidence level for the LC of 20 time bins (Xiang & Jiang 2021).

#### 4 DISCUSSION AND CONCLUSION

By analyzing the above TS maps of SNR G15.9+0.2, we found that the region of SNR G15.9+0.2 has the significant GeV  $\gamma$ -ray radiation with a 2D Gaussian spatial distribution and a significance level of  $6.47\sigma$ . **Its photon flux is  $(4.09 \pm 0.57) \times 10^{-9}$  ph cm $^{-2}$  s $^{-1}$  with  $\Gamma = 2.94 \pm 0.25$ .** We observed that almost all the radio and X-ray contours from SNR G15.9+0.2 are all within the  $2\sigma$  error circle of the best-fit location. In addition, the  $1\sigma$  error circle also contains some contours from the radio and X-ray energy bands. These results suggest that the position of the new  $\gamma$ -ray source well coincides with SNR G15.9+0.2. Next, we analyzed the variability of approximately 12.4 years of the LC and found that the LC exhibits **a hint of weak variation** with a significance level of  $2.69\sigma$ .

We considered leptonic and hadronic scenarios to explain the GeV SED of SNR G15.9+0.2 from this work using a one-zone model from NAIMA (Zabalza 2015, and references therein). Here we assumed leptonic and hadronic particle distributions satisfy the following two particle distributions:

**(1) A power law model (PL):**

$$N(E) = N_0 \left( \frac{E}{E_0} \right)^{-\alpha}, \quad (1)$$

**(2) A power law with an exponential cutoff model (ECPL):**

$$N(E) = N_0 \left( \frac{E}{E_0} \right)^{-\alpha} \exp\left(-\frac{E}{E_{\text{cutoff}}}\right), \quad (2)$$

where  $E_0$  is set to **10 GeV**,  $N_0$  represents the amplitude,  $E$  is the particle energy,  $\alpha$  is the spectral index,  $E_{\text{cutoff}}$  represents the break energy (Aharonian et al. 2006; Ambrogi et al. 2019; Xin et al. 2019; Xiang & Jiang 2021). **In the fit, we used the Bayesian information criterion (BIC) to determine the goodness of fit of the two models (Schwarz 1978; Ambrogi et al. 2019).** The related formula of BIC is  $\log(n)k - 2\log(L)$ , where  $n$  represents the number of the observed data,  $k$  represents the number of parameters of the model, and  $L$  is the maximum likelihood value. We assumed that the radiation fields of the leptonic and hadronic models come from the extended region of the SNR.

For the leptonic scenario, the presence of very-high-energy (VHE) electrons are confirmed in SNRs (e.g., Tanimori et al. 1998), and the GeV and TeV emissions of SNRs are also observed (e.g., Ackermann et al. 2017; Abdalla et al. 2018a). Subsequently, the inverse Compton scattering from leptons was widely used to explain the SEDs of high-energy bands from SNRs (e.g., Tang et al. 2013; Condon et al. 2017; Zeng et al. 2017, 2019, 2021). Therefore, the leptonic model, as a frequently-used model, is considered in the analysis. Additionally, the detection of the characteristic pion-decay signature in IC 443 and W44 confirms that cosmic-ray protons can be accelerated in SNRs (Ackermann et al. 2013). The proportion of proton composition of the observed CR spectrum on Earth is 99%, suggesting that the hadronic contribution for the  $\gamma$ -ray emission from SNRs cannot be ignored (Liu et al. 2015). Recent studies have shown that the multi-band SED of certain SNRs can be better explained when considering the contribution of hadrons than a pure leptonic scenario. E.g., Puppis A (Xin et al. 2017), SNR G106.3+2.7 (Xin et al. 2019; Yang et al. 2021), Kepler's SNR (Xiang & Jiang 2021). Consequently, we also considered the hadronic origin here.

**The interaction between high-energy particles of SNR and the surrounding molecular cloud can serve as the important evidence for the hadronic origin (Wootten 1977; Denoyer 1979; Tatematsu et al. 1990; Green et al. 1997; Reach & Rho 1999; Zhou et al. 2009; Kilpatrick et al. 2014).** Here, we firstly investigated OH maser emission at 1720 MHz around SNR G15.9+0.2 from Green et al. (1997). However, we did not find the significant OH maser emission around SNR G15.9+0.2; thus, there is no convincing evidence to verify the interactions of SNR G15.9+0.2 with "OH" molecular clouds. In addition, Tian et al. (2019) proposed that the region of SNR G15.9+0.2 is likely to produce high-energy emissions, owing to the likely interactions between SNR G15.9+0.2 and the surrounding CO molecular clouds. Subsequently, we quickly investigated the past CO observations from Dame et al. (2001) and Dempsey et al. (2013), and we found dense CO molecular clouds in the  $1\sigma$  error circle of the best-fit position of SNR G15.9+0.2. **However, no broad CO emission lines were observed from the region in their works.** Therefore, the interaction between SNR and surrounding CO molecules is uncertain and needs further observations to verify in the future.

Owing to the uncertainty of the interaction with the surrounding CO molecules, we assumed that the GeV radiation of the SNR comes from the interaction between the high-energy particles inside the forward shock and the surrounding interstellar medium of the SNR, and its related gas density  $n_{\text{gas}} = 0.7 \text{ cm}^{-3}$  (Reynolds et al. 2006). For the distance of SNR G15.9+0.2, we took 8.5 kpc from Reynolds et al. (2006) for fitting the SED. Here, PYTHIA 8, which involves the cross-section of proton-proton interactions and pion production from Kafexhiu et al. (2014), was selected to perform the analysis.

The best-fit results of the two radiation models are shown in the two panels of Figure 5 and Table 2, we found that leptonic and hadronic models with particle distributions of PL and ECPL can explain the SED with a reduced  $\chi^2$  value of approximately 0. Moreover, we found that BIC values of PL and ECPL are close, with the values of approximately 3 and 5, respectively. Therefore, the goodness of fit of PL and ECPL cannot be distinguished thus far. The actual particle distribution of the SNR needs more high-energy observation data to infer in the future (e.g., continuous Fermi-LAT observation above 7 GeV).

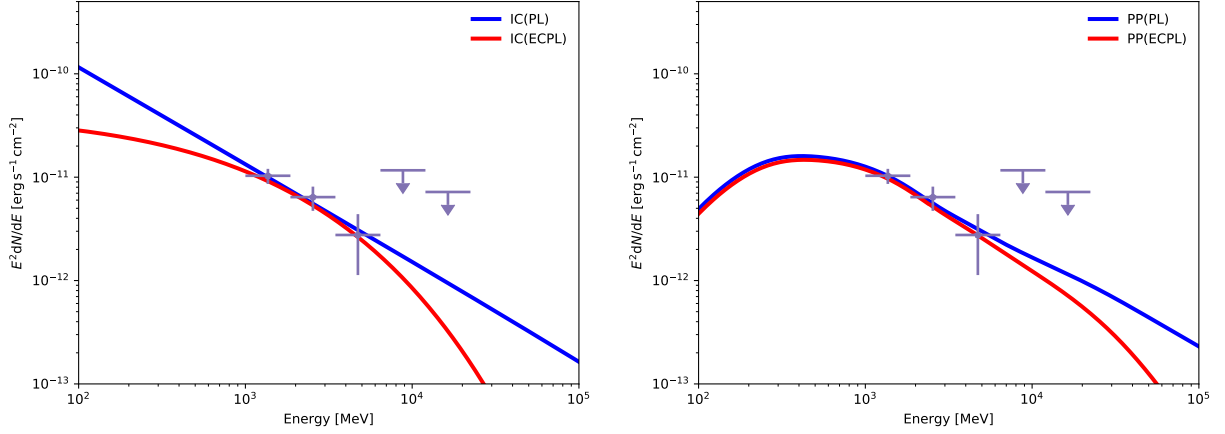


**Figure 5.** For the above two panels, the blue and red solid lines represent the best-fit results of PL and ECPL, respectively. Two upper limits are included in the fitting process. Left panel: the leptonic scenario that is dominated by the inverse Compton scattering. Right panel: the hadronic scenario that is dominated by the decay of neutral pions from the process of proton-proton interactions.

**Table 2.** The Best-fit Parameters of Leptonic and Hadronic Models

Model Name	Particle Distribution	$N_0$	$\alpha$	$E_{\text{cutoff}}$ GeV	$-\log(L)$	BIC	$\chi^2/N_{dof}$
Leptonic model	PL	$4.81^{+1.08}_{-1.25} \times 10^{45}$	$4.87^{+0.07}_{-0.09}$	—	-0.11	3.44	$\frac{0.11 \pm 2}{5-2} = 0.07$
	ECPL	$2.44^{+0.55}_{-0.66} \times 10^{43}$	$2.94^{+0.20}_{-0.23}$	$243.46^{+89.64}_{-68.42}$	-0.03	4.89	$\frac{0.03 \pm 2}{5-3} = 0.03$
Hadronic model	PL	$5.74^{+0.52}_{-0.60} \times 10^{42}$	$2.99^{+0.22}_{-0.20}$	—	-0.13	3.48	$\frac{0.13 \pm 2}{5-2} = 0.09$
	ECPL	$6.17^{+0.93}_{-1.00} \times 10^{42}$	$2.85^{+0.44}_{-0.40}$	$201.81^{+60.81}_{-68.14}$	-0.10	5.03	$\frac{0.10 \pm 2}{5-3} = 0.10$

## ACKNOWLEDGMENT

We sincerely thank the referee for his/her invaluable comments and appreciate the support for this work from the National Key R&D Program of China under Grant No. 2018YFA0404204, the National Natural Science Foundation of China (NSFC U1931113, U1738211, 11303012), the Foundations of Yunnan Province (2018IC059, 2018FY001(-003), 2018FB011), the Scientific Research Fund of Yunnan Education Department (2020Y0039).

## DATA AVAILABILITY

The data underlying this work can be made available in Fermi Science Support Center<sup>9</sup> and will be shared on request to the corresponding author.

## REFERENCES

- Abeyssekara A. U. et al., 2017, APJ, 843, 40  
 Abdalla H. et al., 2018a, A&A, 612, A1  
 Abdollahi S. et al., 2020, ApJS, 247, 33  
 Acero F. et al., 2016b, ApJS, 224, 8  
 Ackermann M. et al., 2013, Sci, 339, 807  
 Ackermann M. et al., 2017, ApJ, 843, 139

<sup>9</sup> <https://heasarc.gsfc.nasa.gov/FTP/fermi/data/lat/weekly/photon/>

- Aharonian F. et al., 2006, *A&A*, 449, 223  
Allen G. E. et al., 1997, *ApJ*, 487, L97  
Allen G.E., Gotthelf E.V., Petre, 1999, in *International Cosmic Ray Conference*, 3, 480  
Ambrogio L., Zanin R., Casanova S., De Oña Wilhelmi E., Peron G., Aharonian F., 2019, *A&A*, 623, A86  
Bell A. R., 1978, *MNRAS*, 182, 147  
Blandford R., Eichler D., 1987, *PhR*, 154, 1  
Caswell J. L., Haynes R. F., Milne D. K., Wellington K. J., 1982, *MNRAS*, 200, 1143  
Condon B., Lemoine-Goumard M., Acero F., Katagiri H., 2017, *ApJ*, 851, 100  
Dame T., Hartmann D., Thaddeus P., 2001, *ApJ*, 547, 792  
Dempsey J. T., Thomas H. S., Currie M. J., 2013, *ApJS*, 209, 8  
Denoyer L. K., 1979a, *ApJL*, 232, L165  
Drury L. O., Aharonian F. A., Völk H. J., 1994, *A&A*, 287, 959  
Dubner G. M., Giacani E. B., Goss W. M., Moffett D. A., & Holdaway M., 1996, *AJ*, 111, 1304  
Finke J.D., Dermer C. D., 2012, *ApJ*, 751, 65  
Green A. J., Frail D. A., Goss W. M., Otrupcek R., 1997, *AJ*, 114, 2058  
H.E.S.S. Collaboration, 2018, *A&A*, 612, A3  
Kafexhiu E., Aharonian F., Taylor A. M., Vila G. S., 2014, *Phys. Rev.*, D90, 123014  
Kilpatrick C. D., Biegging J. H., Rieke G. H., 2014, *ApJ*, 796, 144  
Lande J. et al., 2012, *ApJ*, 756, 5  
Liu B. et al., 2015, *APJ*, 809,102  
Maggi P., Acero F., 2017, *A&A*, 597, A65  
Mattox J. R. et al., 1996, *ApJ*, 461, 396  
Morlino G., Caprioli D., 2012, *AIPC*, 1505, 241  
Nolan P. L. et al., 2012, *ApJS*, 199, 31  
Reach W. T., Rho J., 1999, *ApJ*, 511, 836  
Reynolds S. P. et al., 2006, *ApJ*, 652, L45  
Schwarz G. 1978, *Ann. Stat.*, 6, 461  
Tang Y.Y., Dai Z.C., Zhang L., 2013, *RAA*, 13, 537  
Tanimori T. et al., 1998, *APJ*, 497, L25  
Tatematsu K., Fukui Y., Iwata T., Seward F. D., Nakano M., 1990, *ApJ*, 351, 157  
Tian W. W. et al., 2019, *PASP*, 131, 114301  
Uchiyama Y., Aharonian F. A., Tanaka T., Takahashi T., Maeda Y., 2007, *Nature*, 449, 576  
Virtanen P. et al., 2020, *Nature Methods*, 17, 261  
Vink J., 2012, *A&ARv*, 20, 49  
Wootten H. A., 1977, *ApJ*, 216, 440  
Xiang Y.C., Jiang Z.J., 2021, *APJ*, 908, 22  
Xin Y.L. et al., 2017, 843,90  
Xin Y.L., Zeng H.D., Liu S.M., Fan Y.Z., Wei D.M., 2019, *ApJ*, 885, 162  
Yang C.Y., Zeng H.D., Bao B.W., Zhang L., 2021, preprint (arXiv:2106.02629)  
Zabalza V., 2015, preprint (arXiv:1509.03319)  
Zeng H. et al., 2017, *ApJ*, 834, 153  
Zeng H., Xin Y., Liu S., 2019, *ApJ*, 874, 50  
Zeng H.D., Xin Y.L., Zhang S.N., Liu S.M., 2021, *ApJ*, 910, 78  
Zhang L., Fang J., 2007, *ApJ*, 666, 247  
Zhou X., Chen Y., Su Y., Yang J., 2009, *ApJ*, 691, 516